Hindawi
Geofluids
Volume 2021, Article ID 1194186, 12 pages
https://doi.org/10.1155/2021/1194186

Research Article

Intelligent Microfluidics Research on Relative Permeability Measurement and Prediction of Two-Phase Flow in Micropores

Hongqing Song,[1,2] **Changchun Liu**,[1] **Junming Lao**,[1,2] **Jiulong Wang**,[2,3] **Shuyi Du**,[1,2] **and Mingxu Yu**[4]

[1]*School of Civil and Resource Engineering, University of Science and Technology Beijing, Beijing 100083, China*
[2]*National and Local Joint Engineering Laboratory of Big Data Analysis and Computing Technology, Beijing 100190, China*
[3]*Computer Network Information Center, Chinese Academy of Sciences, Beijing 100190, China*
[4]*Beilong Zeda (Beijing) Data Technology Co., Ltd., Beijing 100190, China*

Correspondence should be addressed to Hongqing Song; songhongqing@ustb.edu.cn

Received 26 October 2021; Revised 18 November 2021; Accepted 22 November 2021; Published 11 December 2021

Academic Editor: Bicheng Yan

Relative permeability is a key index in resource exploitation, energy development, environmental monitoring, and other fields. However, the current determination methods of relative permeability are inefficient and invisible without considering wetting order and pore structure characteristics either. In this study, microfluidic experiments were designed for figuring out key factors impacting on the two-phase relative permeability. The optimized intelligent image recognition was established for saturation extraction. The deep learning was conducted for the prediction of two-phase permeability based on the inputs from microfluidic experiments and image recognition and optimized. Results revealed that phase saturation, wetting order, and pore topology were the key factors influencing the two-phase relative permeability, with the importance of 38.22%, 34.84%, and 26.94%, respectively. The deep learning-based relative permeability model performed well, with MSE < 0.05 and operational efficiency of 3 ms/epoch. Aiming at relative permeability model optimization, on the one hand, the dividing ratio of training set and testing set for flooding phase relative permeability prediction achieved the highest prediction accuracy at 7 : 3, while that for displaced phase was 6 : 4. On the other hand, tanh() activation function performed 40% more accurate than the sigmoid() activation function.

1. Introduction

The relative permeability is a crucial parameter reflecting reservoir rock allocation properties and an indispensable index revealing the characteristics of fluid flow and distribution [1, 2]. Moreover, relative permeability is a key index in resource exploitation, energy development, environmental monitoring, and other fields [3, 4]. The greater the relative permeability of certain fluid in a particular reservoir means that the weaker the reservoir resistance to the fluid, the stronger the mobility of fluid in pores and the more clear the distribution in the reservoir. For instance, in groundwater resource mining and storage, water relative permeability is applied to guide the location of mining sites and to evaluate the risk of groundwater leakage in the reservoir. In oil and gas reservoir development, the relative permeability of crude oil or natural gas is adopted to evaluate the significance and benefits of the reservoir water injection development. In soil environmental monitoring, relative permeability is a key indicator to determine the characteristics of sewage diffusion and transport. The construction of a relative permeability model with high efficiency, high accuracy, high robustness, and extensive applicable scenarios is of great significance to effectively evaluate resource mining efficiency, improve energy recovery, and optimize environmental monitoring and testing [5–8].

The construction of relative permeability models is based on data feedback from adequate relative permeability experiments. However, the current relative permeability determination experiments are still based on the steady-state

multiphase core displacement, which has some shortcomings [9–11]. First, a single core cannot reflect the pore characteristics of the entire reservoir, while equivalent conditional experiments on multiple cores imply significant consumption of time and cost. In addition, the experiments will change the core wetting history or even destroy the internal pore structure of the core, which is not beneficial for improving the experimental accuracy by weakening the stochastic error through multiple experiments. Finally, the experiments require the experimenter to keep recording the flow of each phase fluid and indirectly obtain the saturation at each time, which limits the experimenter resulting in low experimental efficiency [12–15].

Besides, extensive experiments have shown that relative permeability is a function of saturation. Nevertheless, the factors such as wetting order and pore structure characteristics also have negligible effect on relative permeability. Most of the relative permeability models proposed by academia lack the consideration of wetting order and pore structure characteristics. This is largely due to the invisibility of internal flow during conventional steady-state core displacement experiments, leading to the wetting order and the pore structure features' unattainability. In addition, the introduction of wetting order and pore structure characteristics based on the phase saturation will significantly increase the nonlinearity and model complexity of the relative permeability model, which increases the difficulty to build a reliable relative permeability model [16–19].

The nonsteady two-phase microfluidic experiments are characterized by whole-process visualization, automated parameter recording, and the experimental setup closer to the two-phase displacement flow in engineering practice. It is a reliable substitution experiment to obtain the basic data of constructing the relative permeability model. During the microfluidic experiments, the electron ocular records the saturation over time, producing a large number of image data [20–23]. According to the microfluidic experiments, general cognition of impacts from various parameters on relative permeability could be obtained, while the quantitative contribution of each parameter could be clarified basing on the Sobol sensitivity analysis model. Furthermore, by introducing the image recognition algorithm, the intelligent identification, storage and analysis of saturation, wetting order, and pore structure characteristics could be achieved with less time cost comparing to conventional methods [24–27]. Finally, based on the saturation, wetting order, and pore structure data, relative permeability intelligent models are constructed by adopting deep learning algorithm, especially the deep neural network (DNN) [28, 29].

In this study, microfluidic experiments were designed for figuring out key factors impacting on the two-phase relative permeability. The optimized intelligent image recognition was established for saturation extraction. The deep learning was conducted for the prediction of two-phase permeability based on the inputs from microfluidic experiments and image recognition. The microfluidic experiments and deep learning model introduced in this study are of great significance for efficient and reliable research on resource exploitation, energy development, and environmental monitoring.

2. Methodology

The research route for intelligent model-based image recognition and permeability prediction of two-phase flow in micropores is shown in Figure 1. First, experimental images were obtained by the designed microfluidic two-phase flow experiments. Subsequently, the image data was preprocessed via applying the image enhancement algorithm specifically the global equalization. Secondly, the preprocessed image data was input into the convolution neural network (CNN); then, the water and oil saturation in the images was extracted and identified. Output from the CNN, the oil and water saturation together with the wetting order and pore diversity obtained from the microfluidic two-phase flow experiments was input to the deep neural network (DNN) model. Finally, the intelligent prediction model of relative permeability based on the DNN was established and optimized [30–34].

2.1. Physical Equations. In this study, the two-phase flow in micropores specified as the process of oil flooding by water was investigated. The flowing process could be described as the Darcy porous flow [31, 35]. According to the Darcy law, the relationship between the permeability and the pressure and flow, as shown in the following equation [31, 36, 37]:

$$Q = \frac{KA}{\mu}\nabla P, \tag{1}$$

where Q is flow rate, m^3/s; K is the permeability of the porous media, m^2; A is the outlet area, m^2; μ is the viscosity of liquid, Pa·s; and ∇P is the pressure gradient, Pa/m.

Accordingly, the permeability is defined as the format as shown in the following equation:

$$K = \frac{u\mu}{\nabla P}, \tag{2}$$

where u is the liquid velocity, m/s.

Furthermore, the relative permeability of a certain liquid is defined as the format as shown in the following equation:

$$K_{ri} = \frac{u_i\mu_i}{K\nabla P_i}, \tag{3}$$

where K_{ri} is the relative permeability of liquid i, dimensionless; u_i is the velocity of liquid i during multiphase flow, m/s; μ_i is the viscosity of liquid i, Pa·s; and ∇P_i is the pressure gradient on liquid i, Pa/m.

The pressure gradient on liquid i is correlated to the capillary force on which and the absolute driving pressure gradient, as shown in the following equation:

$$\nabla P_i = \frac{P_{c,i} + P_a}{L}, \tag{4}$$

where $P_{c,i}$ is the capillary force on liquid i, Pa; P_a is the absolute driving pressure, Pa; and L is the length of the porous media, m.

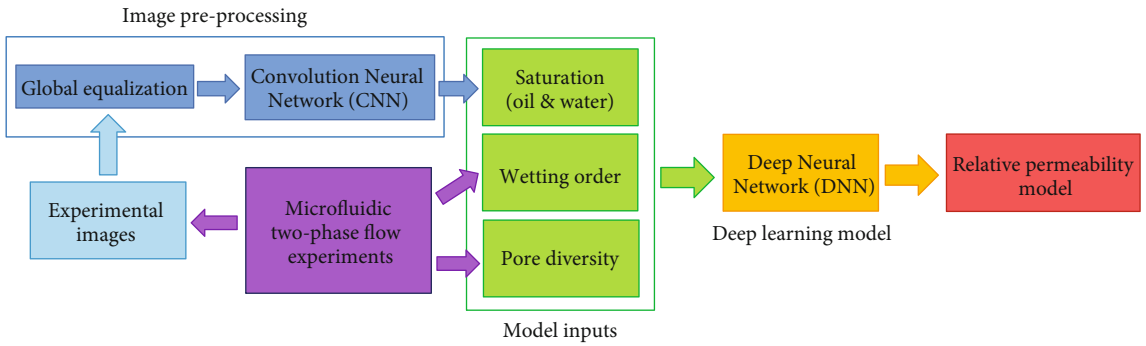

Figure 1: Research route for intelligent model-based image recognition and permeability prediction of two-phase flow in micropores.

2.2. Microfluidic Two-Phase Experiments. The microfluidic two-phase experiments were conducted at a laboratory at room temperature of 24.3°C with 70% relative humidity and reaching stable thermal balance indoors. The atmospheric pressure of the laboratory site was 99.2 kPa. Water used in the experiments was mineral water. Oil used in the experiments was light crude oil. Detailed properties of fluids used in experiments are shown in Table 1. While studying the impact of wetting order on two-phase relative permeability, Light oil $2^{\#}$ was used as flooding phase to flood the mineral water since the microfluidic chips were hydrophobic. Meanwhile, the reason why Light oil $2^{\#}$ as flooding phase was adopted was to maintain the capillary force on either flooding or displaced phase as constant variable. Based on the properties of the experimental fluid, the three-phase porous flow process performed in this research was considered an isothermal incompressible two-dimensional flow [21, 38–40].

The overview of the flooding experiment and data measurement and record is presented in Figure 2. In particular, the driving module, pressure monitoring module, experiment visualization module, and data record module were established. The adopted equipment and materials included two constant-speed microinjection pumps for liquid injection, medical plastic syringes, alloy four-way valve, 16 kPa capsule pressure gauge, PE lines, microfluidic chips, optical microscope with electron lens, waste liquid collection test tube, mobile workstation, and experimental recording camera [41–44]. The left and lower inlets of the four-way valve were connected to the water pump and nitrogen pump, respectively, while the outlet at the top were connected to the pressure gauge and the right outlet connected to the inlet of the microfluidic chip. Before the experiment began, the microfluidic chip was saturated by the displaced phase. The injection rate was also set in the microinjection pump, which corresponded to the injection rate at the inlet of microfluidic chip [36, 45–47].

To quantitatively analyze the contribution of each parameter to relative permeability, the Sobol sensitivity analysis method was adopted. The Sobol method is based on the idea of model decomposition, yielding the sensitivity of parameters 1, 2, and higher, respectively. Usually, 1 sensitivity reflects the main effect of parameters, while 2 and higher sensitivity consider more. Compared with other sensitivity analysis methods, the Sobol method has a relatively stable sampling method, which can grade the sensitivity to the contribution proportion of the output variance through parameters and is a more efficient method to quantitatively identify the sensitivity of different parameters. The specific model of Sobol sensitivity analysis is shown in equations (5)-(9).

$$f(x) = f_0 + \sum_i f_i(x_i) + \sum_{i<j} f_{ij}(x_i, x_j) + \cdots + \sum f_{1,2,\cdots,n}(x_1, x_2, \cdots x_n), \tag{5}$$

$$D = \sum_i D_i + \sum_{i<j} D_{ij} + \cdots + \sum D_{1,2,\cdots,n}, \tag{6}$$

$$S_{1,2,\cdots,n} = \frac{D_{1,2,\cdots,n}}{D}, \tag{7}$$

$$1 = \sum_i S_i + \sum_{i<j} S_{ij} + \cdots + \sum S_{1,2,\cdots,n}, \tag{8}$$

$$S_{Ti} = 1 - \sum S_{\sim i}. \tag{9}$$

2.3. Image Enhancement and Recognition. Before the saturation recognition and extraction, the images require to be enhanced for highlighting the features while weakening the white noise inside. In particular, smoothing is required to eliminate noise interference in the image or to enhance contrast and sometimes to emphasize the edges and details of the image. For oil-water two-phase microfluidic experimental images, the grayscale distribution of the image is relatively concentrated, resulting in the segmentation difficulty of two-phase saturation. Histogram equalization is achieved by adjusting the gray order distribution of the image so that the distribution on the 0~255 gray order is more balanced, which is an effective method to improve the contrast of the image and simplify the segmentation of oil and water saturation. Shown in Figure 3 is a schematic diagram of the histogram equalization principle. Generally, images obtained from oil-water two-phase microfluidic experiments are suitable for adopting the histogram equalization method to enhance image details.

After the image enhancement is done by histogram equalization, the next step is the saturation recognition and extraction. The convolution neural network (CNN) is adopted in this study for oil and water saturation

Table 1: Phase parameters in the injection experiment (at 24.3°C, 99.2 kPa).

Phase type	Material	Density (kg/m^3)	Viscosity (mPa·s)	Compressibility (1/Pa)
Displaced phase	Light oil 1#	855.297	4.160	5.268×10^{-10}
Flooding/displaced phase	Mineral water	997.323	0.917	4.504×10^{-10}
Flooding phase	Light oil 2#	804.865	1.617	5.602×10^{-10}

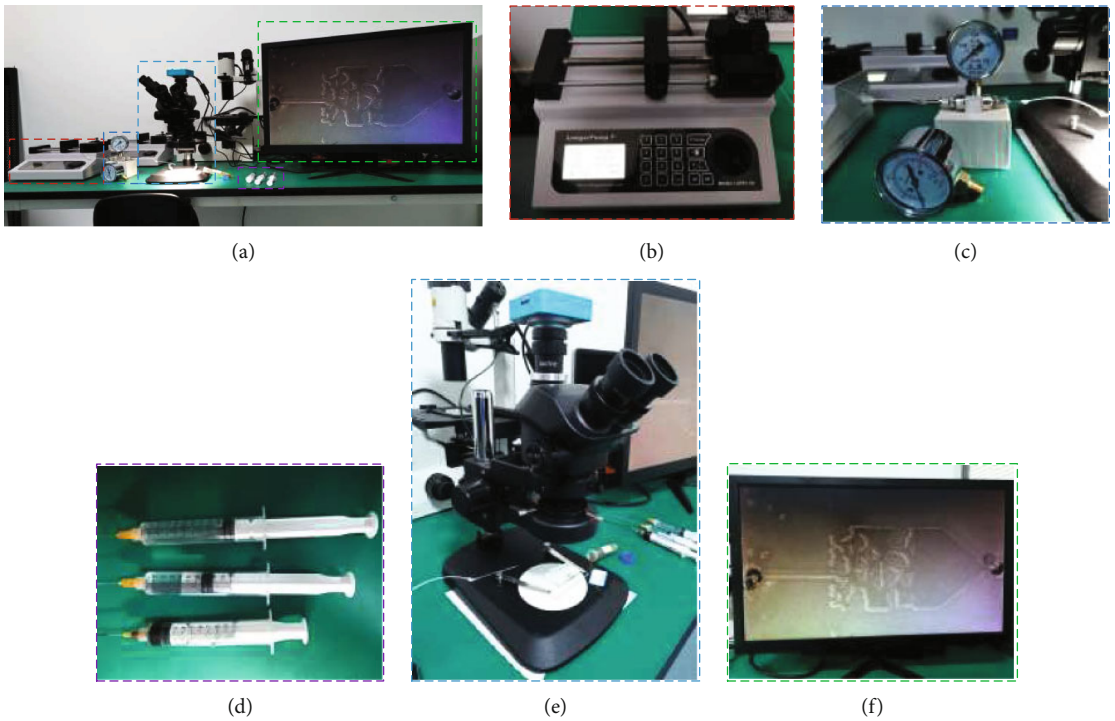

Figure 2: The microfluidic experiment scheme of water-oil flow: (a) overview of experimental equipment; (b) microinjection pump; (c) capsule pressure gauge (16 kPa) and alloy four-way valve; (d) medical plastic syringes; (e) optical microscope with electron lens and microfluidic chip; (f) screen and data record.

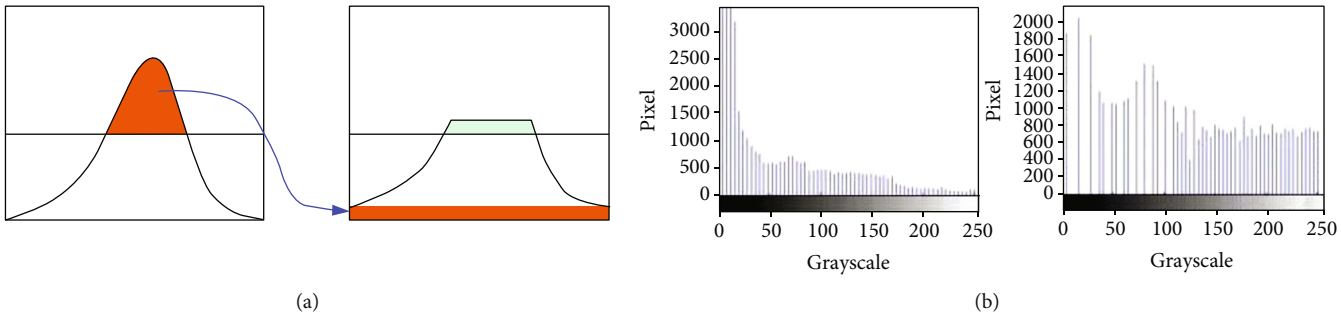

Figure 3: Schematic diagram of the histogram equalization principle. (a) The partial pixels at concentrated grayscale are equally converted to which at diverse grayscale ranging from 0 to 255. (b) The practical processing results based on the principle demonstrated in (a).

recognition and extraction from microfluidic experimental images. The schematic diagram of the CNN is shown in Figure 4. The CNN consists of the following five parts: the input layer, convolution layer, pooling layer, fully connected layer, and the output layer. The key advantage of this method is that it could extract local data features through convolution and pooling operations. Besides, as a supervised intelligent method, the CNN is with high reliability and robustness.

2.4. Deep Learning Model. A narrow definition of deep learning is the neural network with multilayers. Accordingly, the CNN mentioned above and the DNN which is introduced later are both classified as the deep learning model. In this

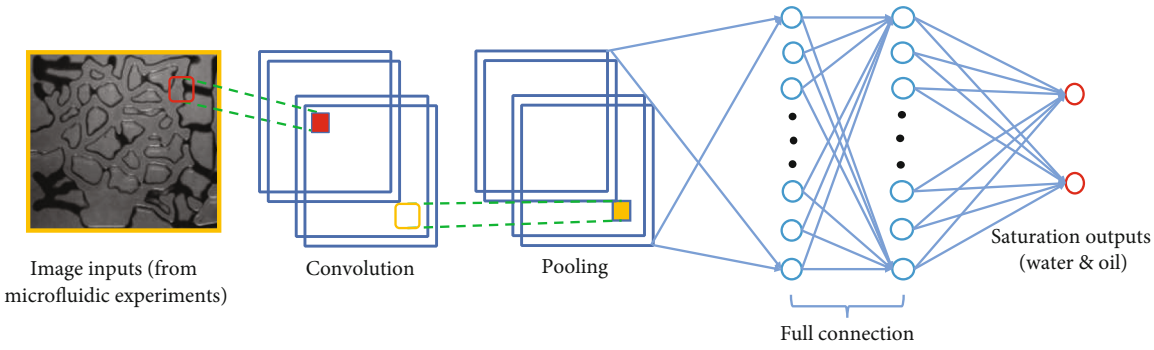

Figure 4: Schematic diagram of the convolution neural network (CNN) for saturation extraction.

study, the deep neural network (DNN) model was proposed for effectively extracting the linear and nonlinear characteristics of the data. The schematic diagram of the DNN for two-phase relative permeability prediction is shown in Figure 5, and the fundamental theories of the DNN are described from equation (10) to equation (14). Specifically, equation (10) to equation (12), respectively, show the operational criterion between the input layer and the first hidden layer, present hidden layer and next hidden layer, and the last hidden layer and output layer, while equation (13) to equation (14) show the activation functions of tanh() and sigmoid(). The parameter matrix of A and b is determined after the DNN is well-trained and validated [48–52].

$$\text{Activation}\left(A^1X + b^1\right) = H^1, \tag{10}$$

$$\text{Activation}\left(A^{n+1}H^n + b^{n+1}\right) = H^{n+1}, \tag{11}$$

$$\text{Activation}\left(A^{N+1}H^N + b^{N+1}\right) = Y, \tag{12}$$

$$\tanh\,(x) = \frac{\exp\,(x) - \exp\,(-x)}{\exp\,(x) + \exp\,(-x)}, \tag{13}$$

$$\text{sigmoid}(x) = \frac{1}{1 + \exp\,(-x)}, \tag{14}$$

where X is the input matrix of this study consisting of saturation, wetting order, and pore diversity; H is the hidden layer matrix; A is the weight matrix while b is the bias matrix, both called the parameter matrix; n is the layer order of the hidden layer; N is the amount of hidden layers; and Y is the output matrix, corresponding to the relative permeability in this study.

In order to control the error of deep learning models during the training learning process, loss function is usually used to reflect the regression training effect of the model. The commonly used loss functions include mean square error (MSE), as shown in equation (15). According to the law of gradient descent and back-propagation of regression error, the parameter matrix A and b are adjusted and a model with high accuracy is finally obtained.

$$\text{MSE} = \frac{1}{M}\sum_{i=1}^{M}\left(y_i^{\text{or}} - y_i^{\text{re}}\right)^2, \tag{15}$$

where M is the total number of the output variable which is the product of variable dimensions and feature numbers; y_i represents the ith output variable, while the superscript or and re represent original value and regressed value, respectively.

For neural networks with multiple input variables, different variables may have different units and values. To eliminate this effect and maintain the relative relationship between the values of the same variables, it is necessary to normalize the input dataset via the following equation:

$$X' = \frac{X - X_{\min}}{X_{\max} - X_{\min}}, \tag{16}$$

where X' is the normalized input matrix; X is the original input matrix; and $X_{\max}$ and $X_{\min}$ are the maximum and minimum values of the input variables.

3. Results and Discussion

3.1. Characterizations of Two-Phase Flow in Micropores. In this study, 12 sets of microfluidic experiments with different pore structure characteristics, wetting order, and injection rate conditions were designed. The experimental results of microfluidic two-phase flow experiments are shown in Figure 6. Figures 6(a)–6(l), respectively, show experimental images at initial injection, during injection, and injection completion of each group of experiment. Among them, Figures 6(a)–6(c) show experiments with the coefficient of pore diversity of 0.872. The injection rate was 50, 100, and 150 μL/min, respectively. The wetting order was mineral water flooding. It should be noted that when mineral water flooded, the Light crude oil $1^{\#}$ was displaced while when Light crude oil $2^{\#}$ flooded, the mineral water was displaced. Similarly, Figures 4(d)–4(f) show experiments with the coefficient of pore diversity of 3.248. The setting of injection rate and wetting order was consistent with the experiments shown from Figures 6(a)–6(c). Figures 4(g)–4(i) show experiments with the coefficient of pore diversity of 6.965. The setting of injection rate and wetting order was consistent with the experiments shown from Figures 6(a)–6(d).

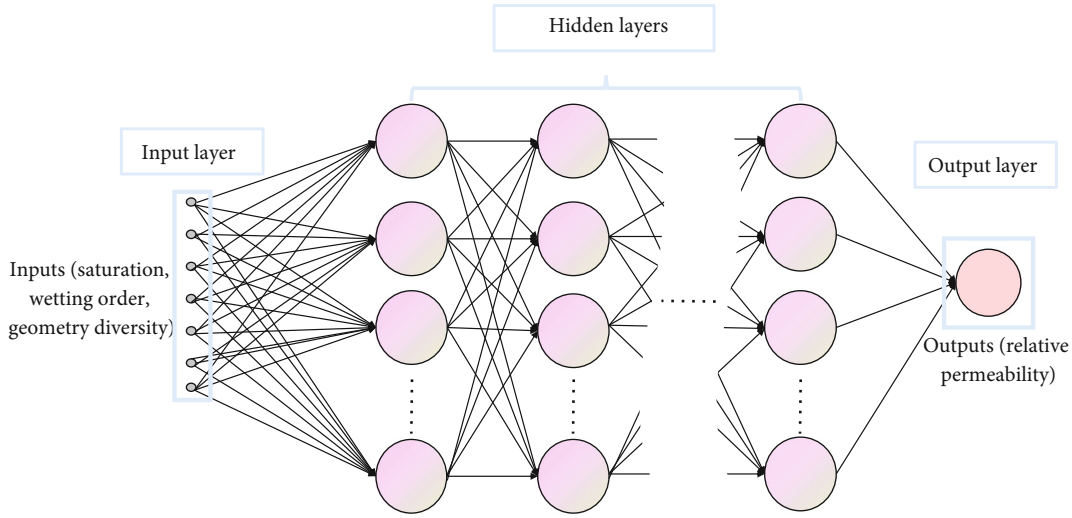

Figure 5: Schematic diagram of the deep neural network (DNN) for two-phase relative permeability prediction.

Figures 4(j)–4(l) show experiments with the coefficient of pore diversity of 0.872, 3.248, and 6.965, respectively. The injection rates were all 100 μL/min. The wetting order was Light crude oil $2^{\#}$ flooding.

According to Figure 6, it could be found that the in addition to the saturation, the wetting order and pore diversity of pores did significantly impact on the two-phase flow in micropores. Hence, the saturation, wetting order, and pore diversity should be contained in the relative permeability model comprehensively.

Though the impact of saturation on relative permeability is hardly possible to visually observe, the effects of wetting order and pore diversity are significantly visible. In particular, at the mineral water flooding condition, it could be seen that the higher pore diversity was conducive to enhance the displacement of displaced phase generally. It is worth noting that the relationship between injection rate and saturation is nonlinear, while at the medium injection rate, 100 μL/min, the most residual displaced phase was left in pores. On the contrary, at the light crude oil flooding condition, the most complete flooding was done at the lowest pore diversity.

The reasons why such phenomena occurred are that on the one hand, the capillary effect is evident during the two-phase flow process in micropores. The pores in microfluidic chips were hydrophobic determined by the materials. When the wetting order was set to be mineral flooding, the mineral water occupied the large pores initially and mainly and seldom permitted into fine pores due to the resistance conducted by capillary force on mineral water. Conversely, when the wetting order was set to be light crude oil flooding, the light crude oil occupied the fine pores initially and immediately and through which the light crude oil escaped instead of occupying the large pores. On the other hand, the saturation of both flooding and displaced phases was governed by Darcy's law of porous flow and capillary effect. Therefore, at a low injection rate particularly 50 μL/min in this study, the capillary effect played the domain role that large pores were more completely occupied. At a high injection rate particularly 150 μL/min in this study, the Darcy law of porous flow performed more significant that flooding phase could permit into partial fine pores with high flooding pressure. Eventually, at the medium injection rate, particularly 100 μL/min in this study, both capillary effect and Darcy's law of porous flow failed to take advantage of themselves resulting in the most suboptimal flooding performance.

According to the microfluidic two-phase flow experiments, the two-phase flow saturation-relative permeability curves were plotted as shown in Figure 7. Specifically, curves from Figure 7(a)–7(l) are corresponding to the experimental results obtained from Figures 6(a)–6(l).

According to Figure 7, it could be found that at the wetting order of mineral water flooding, the equivalent points of relative permeability were all in the interval where the displaced phase saturation was greater than or equal to 0.8. However, at the wetting order of light crude oil flooding, there was no equivalent point of the two phases, while the two-relative permeability interval is shorter than the wetting order of mineral water flooding.

3.2. Sensitivity Analysis of Variable Effects on Relative Permeability. The Sobol full-order weight model was applied to perform the sensitivity analysis of the saturation, wetting order, and pore diversity impact on relative permeability as shown in Figure 8. Notably, due to the saturation of the flooding and displaced phase satisfy the constraints of 1, the present study only considered the displaced phase saturation as the input variable for the Sobol full-order weight model. According to the results of the analysis shown in Figure 8, the saturation has the greatest effect on both the relative permeability of flooding phase and displaced phase. The wetting order was the second key impact factor of the relative permeability followed the saturation. Although the effect of the pore structure characteristics (coefficient of diversity) on the relative permeability was minimal among the three variables, the contribution difference from the saturation was not higher than 50%. Overall, phase

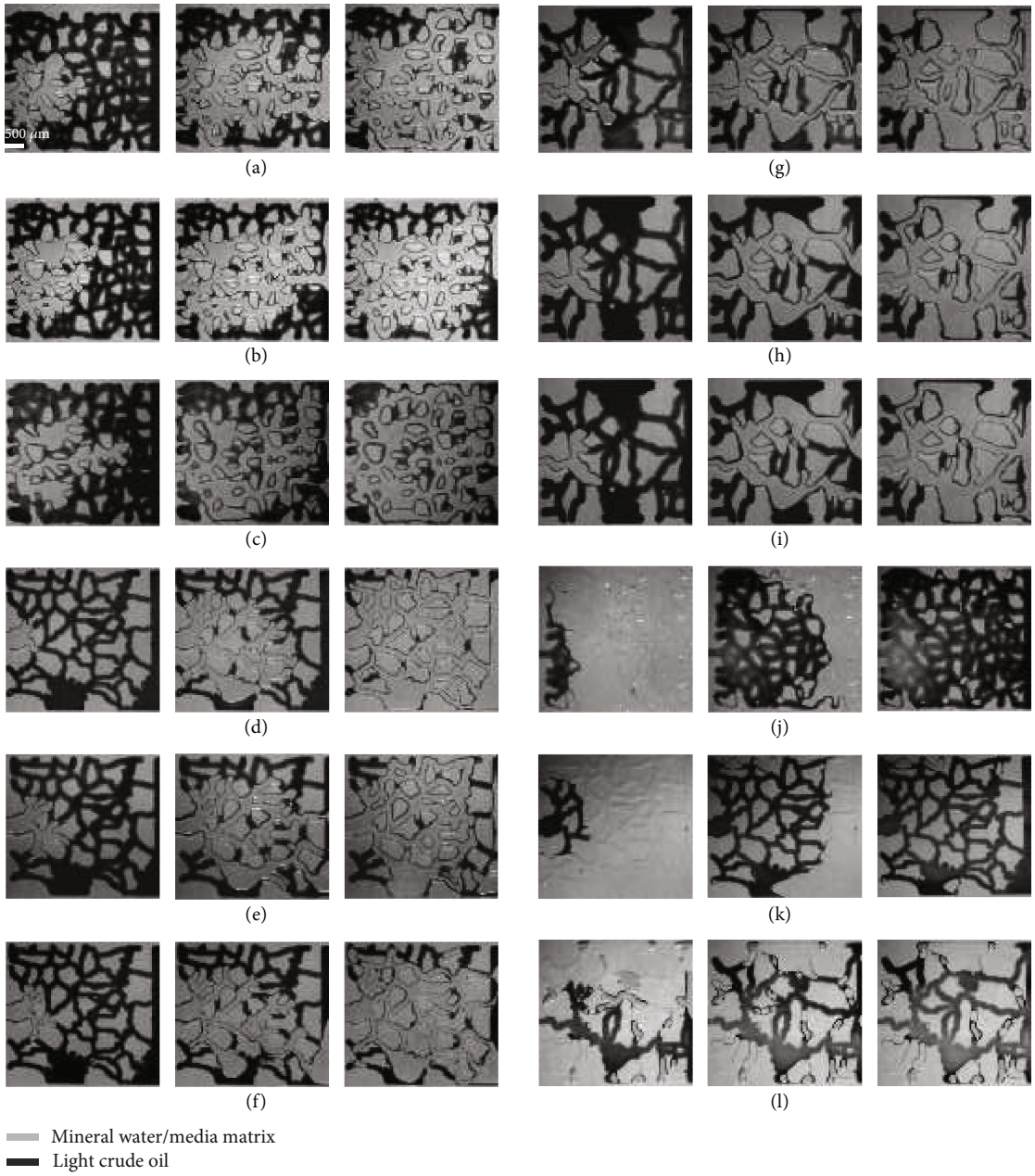

Figure 6: Experimental results of microfluidic two-phase flow experiments.

saturation, wetting order, and pore structure characteristics could be considered key factors in the two-phase flow of oil and water in micropores.

3.3. Performance of Intelligent Relative Permeability Model. The training set of the deep learning-based intelligent relative permeability model was initially divided by the ratio of 8 : 2. The activation function adopted to the model was the tanh() function, and 5 hidden layers were set. The training process and validation results of the intelligent relative permeability model of flooding phase are shown in Figure 9(a), and those of the displaced phase are shown in Figure 9(b).

According to Figures 9(a) and 9(b), it can be found that the training process and validation results of the intelligent relative permeability model of both the flooding phase and displaced phase performed well. Furthermore, Figures 10(a) and 10(b) reveal the specific loss (mean square error, MSE was adopted in this study) at each epoch corresponding to the training process of the intelligent relative permeability model of the flooding phase and displaced phase, respectively. It could be concluded that the intelligent relative permeability models proposed in this study are reliable and accurate.

3.4. Optimization of Intelligent Relative Permeability Model. The intelligent relative permeability model was first optimized by adjusting the dividing ratio of the training set and the test set. As could be seen from the optimization

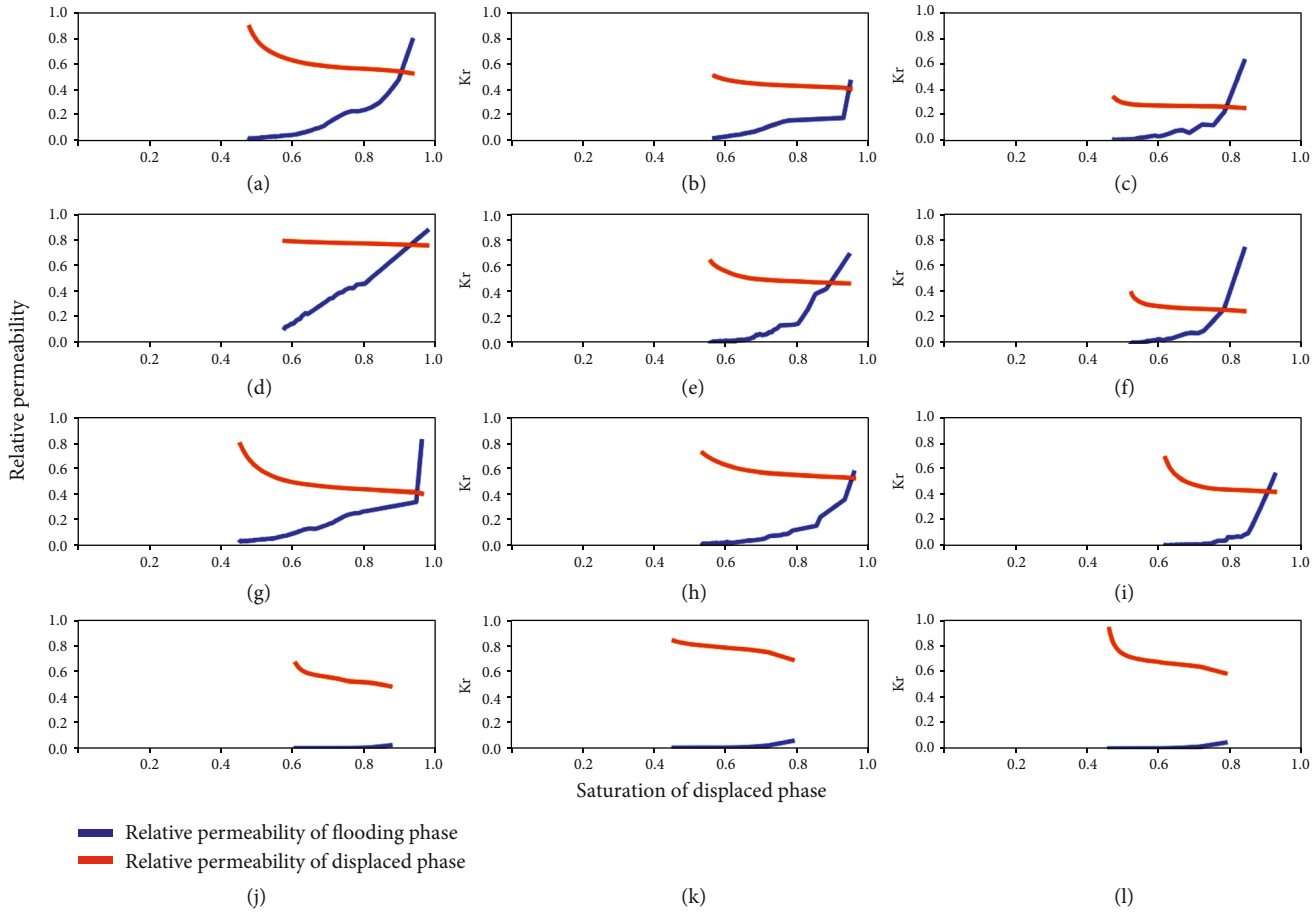

Figure 7: Two-phase relative permeability obtained from microfluidic experiments.

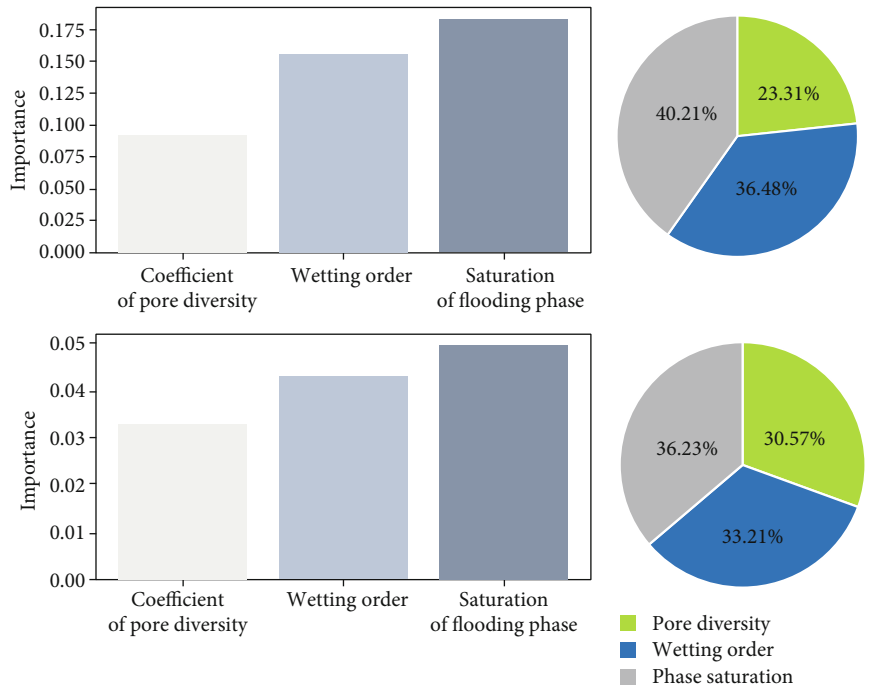

Figure 8: Sobol sensitivity analysis of saturation, wetting order, and pore diversity impact on relative permeability.

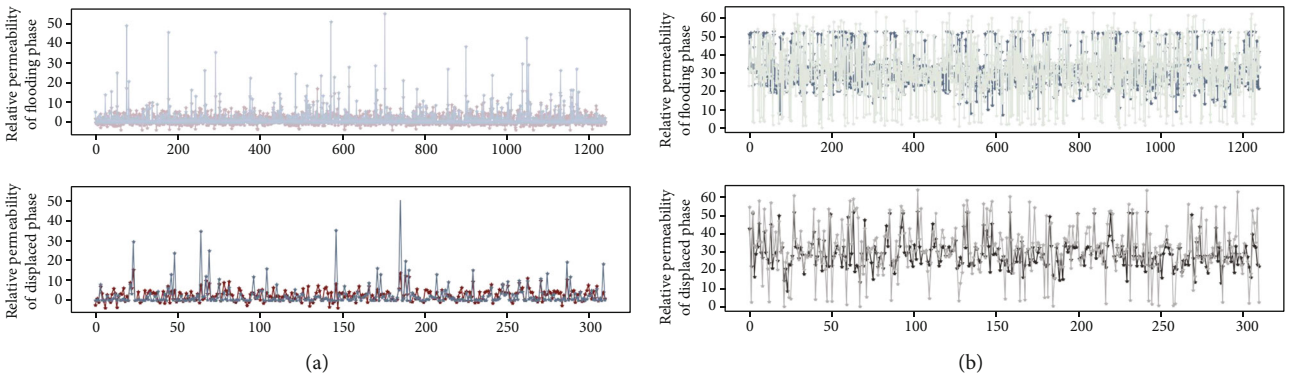

Figure 9: The training and testing results of the DNN: (a) the training process and validation results of the intelligent relative permeability model of the flooding phase; (b) the training process and validation results of the intelligent relative permeability model of the displaced phase.

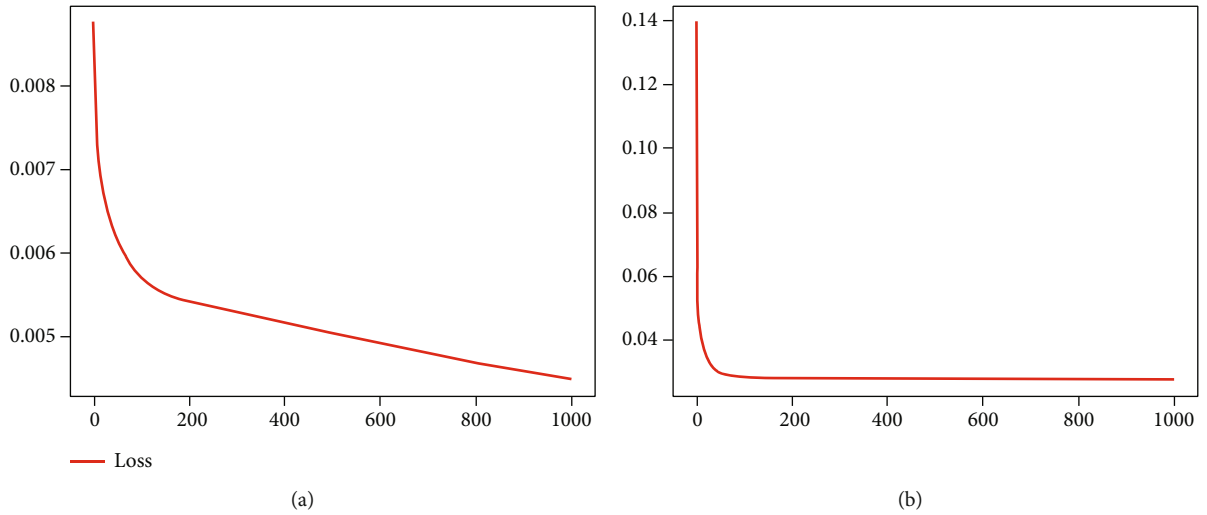

Figure 10: The specific loss (MSE) at each epoch corresponding to the training process of the intelligent relative permeability model of the flooding phase and displaced phase, respectively. (a) The specific loss (MSE) at each epoch corresponding to the training process of the intelligent relative permeability model of the flooding phase. (b) The specific loss (MSE) at each epoch corresponding to the training process of the intelligent relative permeability model of the displaced phase.

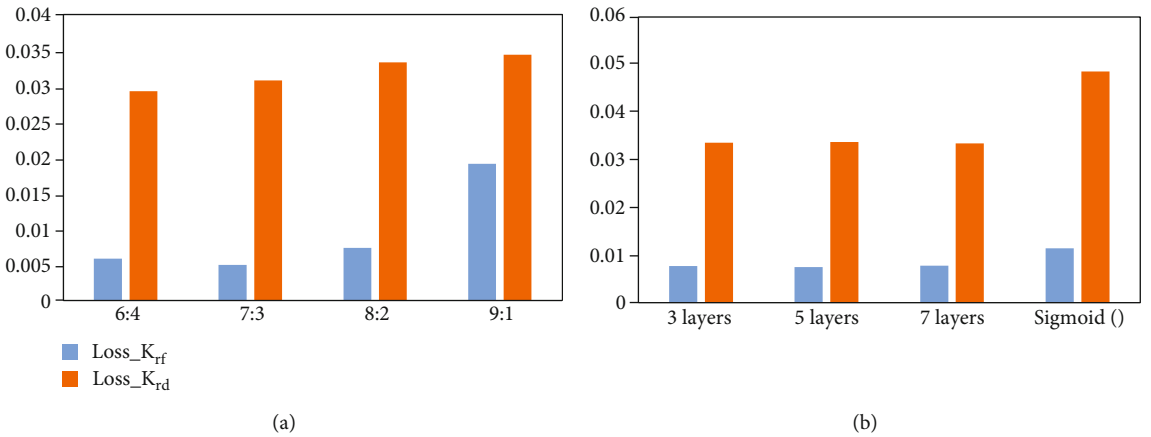

Figure 11: Optimization results of two-phase seepage intelligent model of oil and water. (a) The optimization results of intelligent relative permeability model by adjusting the dividing ratio of the training set and the test set. (b) The optimization results of intelligent relative permeability model by adjusting the number of hidden layers of the deep neural network as well as the activation function.

results in Figure 11(a), the lowest validation loss (MSE) for relative permeability of the flooding phase was at the ratio of 7 : 3 while that for the displaced phase was at the ratio of 6 : 4 compared to the ratio of 8 : 2 for the initial model. Moreover, as the proportion of the training set increased along with the test set scale decreased, the verification loss of the displaced phase relative permeability continuously improved, while that of the flooding phase showed a parabolic trend of falling first and then rising.

Subsequently, the intelligent relative permeability model was optimized by adjusting the number of hidden layers of the deep neural network as well as the activation function. The optimization results in Figure 11(b) show that the adoption of 3 or 7 hidden layers does not bring an obvious optimization effect for the model compared to the initial neural network structure of 5 hidden layers. However, it is worth noting that the tanh() activation function performed 40% more accurate than the sigmoid() activation function while adopting the equivalent 5 hidden layers.

4. Conclusion

Relative permeability is a key index in resource exploitation, energy development, environmental monitoring, and other fields. However, the current determination methods of relative permeability are inefficient and invisible without considering wetting order and pore structure characteristics either. In this study, microfluidic experiments were designed for figuring out key factors impacting on the two-phase relative permeability. The optimized intelligent image recognition was established for saturation extraction. The deep learning was conducted for the prediction of two-phase permeability based on the inputs from microfluidic experiments and image recognition and optimized.

Results revealed that phase saturation, wetting order, and pore topology were the key factors influencing the two-phase relative permeability, with the importance of 38.22%, 34.84%, and 26.94%, respectively. The deep learning model for relative permeability prediction performed well, with MSE < 0.05 and operational efficiency of 3 ms/epoch. Aiming at relative permeability model optimization, on the one hand, the dividing ratio of training set and testing set for flooding phase relative permeability prediction achieved the highest prediction accuracy at 7 : 3, while that for displaced phase was 6 : 4. On the other hand, tanh() activation function performed 40% more accurate than the sigmoid() activation function.

Data Availability

Data is available on request. Please contact the corresponding author for the underlying data supporting the results of the research.

Conflicts of Interest

The authors declare that there is no conflict of interest regarding the publication of this article.

Acknowledgments

This research was supported by the National Natural Science Foundation of China (Grant No. 11972073).

References

[1] Y. Da Wang, R. T. Armstrong, and P. Mostaghimi, "Boosting resolution and recovering texture of 2D and 3D micro-CT images with deep learning," *Water Resources Research*, vol. 56, no. 1, 2020.

[2] J. Zhang, H. Q. Song, W. Y. Zhu, and J. L. Wang, "Liquid transport through nanoscale porous media with strong wettability," *Transport in Porous Media*, vol. 140, no. 3, pp. 697–711, 2021.

[3] F. O. Alpak, M. Araya–Polo, and K. Onyeagoro, "Simplified dynamic modeling of faulted turbidite reservoirs: a deep-learning approach to recovery-factor forecasting for exploration," *SPE Reservoir Evaluation & Engineering*, vol. 22, no. 4, pp. 1240–1255, 2019.

[4] N. J. Alqahtani, T. Chung, Y. D. Wang, R. T. Armstrong, P. Swietojanski, and P. Mostaghimi, "Flow-based characterization of digital rock images using deep learning," *SPE Journal*, vol. 26, no. 4, pp. 1800–1811, 2021.

[5] Z. Zhong, A. Y. Sun, Y. Y. Wang, and B. Ren, "Predicting field production rates for waterflooding using a machine learning-based proxy model," *Journal of Petroleum Science and Engineering*, vol. 194, article 107574, 2020.

[6] B. C. Yan, L. D. Mi, Y. H. Wang, H. W. Tang, C. An, and J. E. Killough, "Multi-porosity multi-physics compositional simulation for gas storage and transport in highly heterogeneous shales," *Journal of Petroleum Science and Engineering*, vol. 160, pp. 498–509, 2018.

[7] B. C. Yan, L. D. Mi, Z. Chai, Y. H. Wang, and J. E. Killough, "An enhanced discrete fracture network model for multiphase flow in fractured reservoirs," *Journal of Petroleum Science and Engineering*, vol. 161, pp. 667–682, 2018.

[8] O. Santamaria, S. H. Lopera, M. Riazi, M. Minale, F. B. Cortes, and C. A. Franco, "Phenomenological study of the micro- and macroscopic mechanisms during polymer flooding with SiO_2 nanoparticles," *Journal of Petroleum Science and Engineering*, vol. 198, p. 108135, 2021.

[9] P. Purswani, Z. T. Karpyn, K. Enab, Y. Xue, and X. L. Huang, "Evaluation of image segmentation techniques for image-based rock property estimation," *Journal of Petroleum Science and Engineering*, vol. 195, article 107890, 2020.

[10] A. Gerami, R. T. Armstrong, Y. Jing, F. A. Wahid, H. Arandiyan, and P. Mostaghimi, "Microscale insights into gas recovery from bright and dull bands in coal," *Journal of Petroleum Science and Engineering*, vol. 172, pp. 373–382, 2019.

[11] O. D. Arigbe, M. B. Oyeneyin, I. Arana, and M. D. Ghazi, "Real-time relative permeability prediction using deep learning," *Journal of Petroleum Exploration and Production Technology*, vol. 9, no. 2, pp. 1271–1284, 2019.

[12] J. W. Sanders, H. S. M. Chen, J. M. Johnson et al., "Synthetic generation of DSC-MRI-derived relative CBV maps from DCE MRI of brain tumors," *Magnetic Resonance in Medicine*, vol. 85, no. 1, pp. 469–479, 2021.

[13] W. S. Loos, R. Souza, L. B. Andersen, R. M. Lebel, and R. Frayne, "Extraction of a vascular function for a fully automated dynamic contrast-enhanced magnetic resonance brain

image processing pipeline," *Magnetic Resonance in Medicine*, 2021.

[14] H. Q. Song, H. H. Guo, Y. H. Wang et al., "A novel hybrid energy system for hydrogen production and storage in a depleted oil reservoir," *International Journal of Hydrogen Energy*, vol. 46, no. 34, pp. 18020–18031, 2021.

[15] S. A. Mahoney, T. E. Rufford, V. Rudolph, K. Y. Liu, S. Rodrigues, and K. M. Steel, "Creation of microchannels in Bowen Basin coals using UV laser and reactive ion etching," *International Journal of Coal Geology*, vol. 144, pp. 48–57, 2015.

[16] P. Mostaghimi, R. T. Armstrong, A. Gerami et al., "Cleat-scale characterisation of coal: an overview," *Journal of Natural Gas Science and Engineering*, vol. 39, pp. 143–160, 2017.

[17] J. C. Lv, K. P. Xue, Z. D. Zhang, Z. C. Cheng, Y. Liu, and H. L. Mu, "Pore-scale investigation of hydrate morphology evolution and seepage characteristics in hydrate bearing microfluidic chip," *Journal of Natural Gas Science and Engineering*, vol. 88, p. 103881, 2021.

[18] L. Chen, W. B. Lin, P. Chen, S. Jiang, L. Liu, and H. Y. Hu, "Porosity prediction from well logs using back propagation neural network optimized by genetic algorithm in one heterogeneous oil reservoirs of Ordos Basin, China," *Journal of Earth Science*, vol. 32, no. 4, pp. 828–838, 2021.

[19] H. Q. Song, J. J. Xu, J. Fang, Z. G. Cao, L. Z. Yang, and T. X. Li, "Potential for mine water disposal in coal seam goaf: investigation of storage coefficients in the Shendong mining area," *Journal of Cleaner Production*, vol. 244, p. 118646, 2020.

[20] C. A. Browne, A. Shih, and S. S. Datta, "Pore-scale flow characterization of polymer solutions in microfluidic porous media," *Small*, vol. 16, no. 9, p. 1903944, 2020.

[21] G. Grisanti, D. Caprini, G. Sinibaldi et al., "A microfluidic platform for cavitation-enhanced drug delivery," *Micromachines*, vol. 12, no. 6, p. 658, 2021.

[22] W. J. Yun, C. M. Ross, S. Roman, and A. R. Kovscek, "Creation of a dual-porosity and dual-depth micromodel for the study of multiphase flow in complex porous media," *Lab on a Chip*, vol. 17, no. 8, pp. 1462–1474, 2017.

[23] J. F. Wong and C. A. Simmons, "Microfluidic assay for the on-chip electrochemical measurement of cell monolayer permeability," *Lab on a Chip*, vol. 19, no. 6, pp. 1060–1070, 2019.

[24] H. Y. Wu, W. Z. Fang, Q. J. Kang, W. Q. Tao, and R. Qiao, "Predicting effective diffusivity of porous media from images by deep learning," *Scientific Reports*, vol. 9, no. 1, article 20387, 2019.

[25] Z. N. Wu, Y. H. Zhou, H. L. Wang, and Z. H. Jiang, "Depth prediction of urban flood under different rainfall return periods based on deep learning and data warehouse," *Science of the Total Environment*, vol. 716, article 137077, 2020.

[26] A. Riaz, R. P. Gandhiraman, I. K. Dimov et al., "Reactive deposition of nano-films in deep polymeric microcavities," *Lab on a Chip*, vol. 12, no. 22, pp. 4877–4883, 2012.

[27] K. Osei-Bonsu, S. Khorsandi, and M. Piri, "Quantitative analysis of phase topology evolution during three-phase displacements in porous media," *Lab on a Chip*, vol. 20, no. 14, pp. 2495–2509, 2020.

[28] P. Kang, J. M. Lao, M. X. Yu, H. Q. Song, and C. Wang, "Reliable prediction on emerging energy supply for National Sustainability and stability: a case study on coal bed gas supply in China based on the dual-LSTM model," *IEEE Access*, vol. 9, pp. 100694–100707, 2021.

[29] S. Du, R. F. Wang, C. J. Wei et al., "The connectivity evaluation among wells in reservoir utilizing machine learning methods," *IEEE Access*, vol. 8, pp. 47209–47219, 2020.

[30] Y. A. Alzahid, P. Mostaghimi, S. D. C. Walsh, and R. T. Armstrong, "Flow regimes during surfactant flooding: the influence of phase behaviour," *Fuel*, vol. 236, pp. 851–860, 2019.

[31] A. H. Alizadeh, M. Khishvand, M. A. Ioannidis, and M. Piri, "Multi-scale experimental study of carbonated water injection: an effective process for mobilization and recovery of trapped oil," *Fuel*, vol. 132, pp. 219–235, 2014.

[32] M. Yue, X. H. Huang, F. M. He, L. Z. Yang, W. Y. Zhu, and Z. X. Chen, "Analysis of the influence of different fracture network structures on the production of shale gas reservoirs," *Geofluids*, vol. 2020, Article ID 8870429, 11 pages, 2020.

[33] M. Yue, W. Y. Zhu, H. Y. Han, H. Q. Song, Y. Q. Long, and Y. Lou, "Experimental research on remaining oil distribution and recovery performances after nano-micron polymer particles injection by direct visualization," *Fuel*, vol. 212, pp. 506–514, 2018.

[34] M. Yue, W. Y. Zhu, Z. Y. Song, Y. Q. Long, and H. Q. Song, "Study on distribution of reservoir endogenous microbe and oil displacement mechanism," *Saudi Journal of Biological Sciences*, vol. 24, no. 2, pp. 263–267, 2017.

[35] H. Q. Song, J. Zhang, D. D. Ni et al., "Investigation on in-situ water ice recovery considering energy efficiency at the lunar south pole," *Applied Energy*, vol. 298, p. 117136, 2021.

[36] J. L. Wang, H. Q. Song, and Y. H. Wang, "Investigation on the micro-flow mechanism of enhanced oil recovery by low- salinity water flooding in carbonate reservoir," *Fuel*, vol. 266, article 117156, 2020.

[37] Q. T. Zhang, C. J. Wei, Y. H. Wang, S. Du, Y. C. Zhou, and H. Q. Song, "Potential for prediction of water saturation distribution in reservoirs utilizing machine learning methods," *Energies*, vol. 12, no. 19, p. 3597, 2019.

[38] N. Wang, Y. Tang, Y. Wu et al., "Dynamic evolution of microstructure morphology in thin-sample solidification: deep learning assisted synchrotron X-ray radiography," *Materials Characterization*, vol. 181, p. 111451, 2021.

[39] S. A. Mahoney, T. E. Rufford, D. Johnson et al., "The effect of rank, lithotype and roughness on contact angle measurements in coal cleats," *International Journal of Coal Geology*, vol. 179, pp. 302–315, 2017.

[40] A. Gerami, P. Mostaghimi, R. T. Armstrong, A. Zamani, and M. E. Warkiani, "A microfluidic framework for studying relative permeability in coal," *International Journal of Coal Geology*, vol. 159, pp. 183–193, 2016.

[41] A. Thomas, S. Q. Wang, S. Sohrabi et al., "Characterization of vascular permeability using a biomimetic microfluidic blood vessel model," *Biomicrofluidics*, vol. 11, no. 2, article 024102, 2017.

[42] S. Perez-Rodriguez, S. A. Huang, C. Borau, J. M. Garcia-Aznar, and W. J. Polacheck, "Microfluidic model of monocyte extravasation reveals the role of hemodynamics and subendothelial matrix mechanics in regulating endothelial integrity," *Biomicrofluidics*, vol. 15, no. 5, article 054102, 2021.

[43] T. Scherr, G. L. Knapp, A. Guitreau et al., "Microfluidics and numerical simulation as methods for standardization of zebrafish sperm cell activation," *Biomedical Microdevices*, vol. 17, no. 3, p. 65, 2015.

[44] Q. Ramadan and L. Jing, "Characterization of tight junction disruption and immune response modulation in a miniaturized Caco-2/U937 coculture-based in vitro model of the human intestinal barrier," *Biomedical Microdevices*, vol. 18, no. 1, 2016.

[45] T. Zhang and S. Y. Sun, "A coupled lattice Boltzmann approach to simulate gas flow and transport in shale reservoirs with dynamic sorption," *Fuel*, vol. 246, pp. 196–203, 2019.

[46] L. Z. Yang, J. J. Xu, J. Fang, Z. G. Cao, T. X. Li, and H. Q. Song, "Risk evaluation of groundwater leakage in coal seam goaf: a case study in the Lingxin Mining Area," *Environmental Science and Pollution Research*, vol. 27, no. 21, pp. 26066–26078, 2020.

[47] K. Xu, D. Agrawal, and Q. Darugar, "Hydrophilic nanoparticle-based enhanced oil recovery: microfluidic investigations on mechanisms," *Energy & Fuels*, vol. 32, no. 11, pp. 11243–11252, 2018.

[48] H. Q. Song, S. du, R. F. Wang et al., "Potential for vertical heterogeneity prediction in reservoir basing on machine learning methods," *Geofluids*, vol. 2020, Article ID 3713525, 12 pages, 2020.

[49] J. Z. Liu, "Potential for evaluation of interwell connectivity under the effect of intraformational bed in reservoirs utilizing machine learning methods," *Geofluids*, vol. 2020, Article ID 1651549, 10 pages, 2020.

[50] Y. D. Wang, M. J. Blunt, R. T. Armstrong, and P. Mostaghimi, "Deep learning in pore scale imaging and modeling," *Earth-Science Reviews*, vol. 215, article 103555, 2021.

[51] Y. M. Liu, S. J. Chen, K. Sagoe-Crentsil, and W. H. Duan, "Predicting the permeability of consolidated silty clay via digital soil reconstruction," *Computers and Geotechnics*, vol. 140, article 104468, 2021.

[52] T. Zhang, Y. Li, Y. T. Li, S. Y. Sun, and X. Gao, "A self-adaptive deep learning algorithm for accelerating multi-component flash calculation," *Computer Methods in Applied Mechanics and Engineering*, vol. 369, article 113207, 2020.